Internal Flow Phenomena of Two-Way Contra-Rotating Axial Flow Pump-Turbine in Pump Mode under Variable Speed

C. An[1], Y. Chen[1], R. Zhu[1†], X. Wang[1], Y. Yang[2] and J. Shi[3]

[1] *National Research Center of Pumps, Jiangsu University, Zhenjiang 212013, Jiangsu, China*
[2] *College of Hydraulic Science and Engineering, Yangzhou University, Yangzhou 225009, Jiangsu, China*
[3] *School of Mechanical Engineering, Sichuan University of Science & Engineering, Zigong 643000, China*

† *Corresponding Author Email: ujs_zrs@163.com*

ABSTRACT

This paper investigated the variable speed operation of a two-way contra-rotating axial flow pump–turbine in pump mode. When counter-rotating impellers operate at the same speed, a significant difference exists in the shaft power of the two impellers, thereby causing difficulties in motor selection. However, the same motor is required for both impellers in two-way pump–turbines. To solve this problem, this paper aims to determine the appropriate speed at which the two impellers operate with a similar shaft power. Accordingly, improving the performance of the tidal unit while enabling the basic functions of the pump–turbine is of considerable engineering and academic significance. An analysis of performance variations of the front and rear impellers in the pump mode reveals the law of power variation for each impeller at different speeds of the rear impeller. Under different flow conditions, shaft power of the rear impeller is found to be at least 31% higher compared with that of the front impeller. This result provides practical reference for further research on the operation of counter-rotating axial flow pump–turbine.

NOMENCLATURE

Symbols

Q	volume flow rate	$\vec{\omega}$	vorticity
H	head	$\vec{u}$	velocity
n	rated speed of impeller	V	kinematic viscosity
n_s	specific speed	P_e	shaft power of the impeller
p	pressure	S_{tr}	location of the point corresponding to the pressure value
u_i	velocity in the i direction		
μ	laminar dynamic viscosity		*Abbreviations*
μ_T	turbulent eddy dynamic viscosity	LE	Leading Edge
ρ	the 25℃ water density	TE	Trailing Edge
δ_{ij}	Kronecker delta	PS	Pressure Surface
∇	Hamiltonian operator	SS	Suction Surface

1. INTRODUCTION

Interest in finding and producing sustainable energy alternatives is currently emerging, as awareness of the adverse environmental impact of fossil energy sources increases (Sangiuliano 2017; Li *et al.* 2011; Qian *et al.* 2019). The vast resources of marine energy will contribute to our future energy needs (Charlier 2003; Kim *et al.* 2012). Of the known marine renewable energy sources, waves and tides are two different types of resources considered available and have the potential to generate electricity in the future. In particular, tidal power stations have a relatively long history of using artificially created tidal phase differences and flowing through turbines to generate energy in the

form of electricity (Neill *et al.* 2018; Angeloudis and Falconer 2017). Early tidal studies have concentrated on traditional one-way or two-way operation but without the option of pumping (Prandle 1984; Burrows *et al.* 2009; Xia *et al.* 2010). With the further development of tidal power stations, several scholars have studied energy gains that can result from pumping conditions (Mackay and Hafemeister 2010; Yates *et al.* 2013). Yates *et al.* (2013) indicated that with the addition of finite flow velocities, finite turbine, and sluice capacities, pumped energy gain is 6% at best with the same turbine and pump efficiencies. From an economic point of view, it can pump water at low price times to store energy for use at high prices (Harcourt *et al.* 2019). Therefore, current units used in tidal power plants are mostly reversible pump–turbines, which have six functions of two-way power generation, two-way pumping, and two-way sluice, as shown in Fig. 1 (Burrows *et al.* 2009).
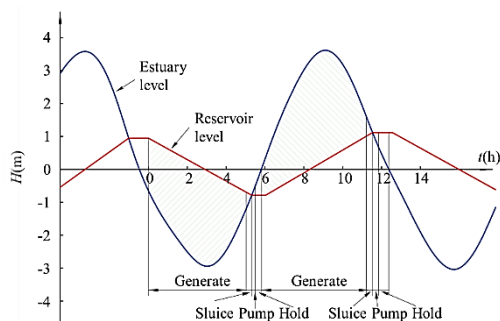
Fig. 1. Six working conditions of tidal power station.

Due to the operating circumstances of tidal power stations, the utilized reversible pump turbines are forced into frequent switches between pumping and power generation modes. Therefore, one of the most important research focuses is the flow instability of the unit. Tiwari *et al.* (2022) evaluated surface roughness effects on the cavitation performance of a low head turbine computationally. Yu *et al.* (2021) focused on revealing the correlation mechanism of blade vortex evolution and energy production in order to analyze the severe pressure fluctuations in the runner. Mao *et al.* (2022) increased the internal fluid stability of pump turbine by reducing the change rate of pressure and improving flow regime. At off-design conditions, undesirable flow with vortex rope also will lead to operating system instability (Kim *et al.* 2022). Yu *et al.* (2022) analyzed cavitation's contribution in energy loss of the pump turbines through entropy generation theory. However, most of the above studies have been carried out on pump turbines with low head and the literature on counter-rotating pump turbines is still scarce.

At present, most research on contra-rotating machinery has focused on fans and marine current turbines. The University of Strathclyde developed a novel contra-rotating tidal turbine and found that reasonably good moored turbine stability within a real tidal stream can be achieved (Clarke *et al.* 2009). Clarke *et al.* (2007) illustrated the design approach

for downstream rotors by considering the flow angle from upstream rotor. Denantes and Bilgen (2006) determined that the efficiency of counter-rotating turbines may be better than single-stage turbines in various operating conditions. Mistry and Pradeep (2013) explored the effect of axial spacing between rotors and found that the off-design speed combinations for rotor-1 and rotor-2 gives different flow behavior with variation of axial spacing. They also determined that high rotational speed of rotor-2 enables improved performance of the stage (Mistry and Pradeep 2014). Airbus conducted research on a contra-rotating open rotor propulsion system and expected to achieve near-improvement in efficiency compared with modern turbofan engines (Stuermer and Akkermans 2014).

Similar with other contra-rotating machinery, contra-rotating axial flow pumps remarkably contribute to energy conversion, reduction of pump size, and improved hydraulic and cavitation performances (Furukawa *et al.* 2007, 2009; Shigemitsu *et al.* 2005; Cao *et al.* 2013). Through further improvements, it meets the conditions of a two-way operation. This paper's research object is a two-way contra-rotating axial flow pump–turbine, which has a superior prospect of the application of tidal power plant. However, only a few studies have been conducted on contra-rotating axial flow pump-turbine, thereby prompting us to analyze studies on contra-rotating axial flow fans. These studies (Sun 2018; Zhang 2015; Ai *et al.* 2017; Ai *et al.* 2016) have shown that the special structure easily causes overload, high pressure, and low efficiency of rear motor during the actual operation process. The inter-stage clearance of the impeller can be adjusted or the angle of the impeller blade is adjustable to improve the performance of the rear impeller. Accordingly, changing the rotational speed of the two-stage impeller can also affect the load distribution, internal flow characteristics, and unit efficiency of the two-stage impeller.

Therefore, the research on the variable speed condition of the unit with contra-rotating structure is significant for improving the performance of the unit. Liu *et al.* (2012) found that the change of performance of the rear rotor is markedly sensitive to the change of speed by studying the internal flow of the contra-rotating axial flow fan under different speeds. Ravelet *et al.* (2018) experimentally studied the effects of the ratio change of load distribution and speed of the two-stage rotor on the performance of the contra-rotating axial flow fan. Li Changnian (Li 2016) studied the performance of the contra-rotating axial flow fan with variable speeds of the two-stage impeller under different flow rates. The preceding study also analyzed the deformation and stress changes of the impeller blade under different working conditions and variable speeds.

Given the preceding research, this research used the numerical simulation method to study and analyze the performance, impeller pressure, and power characteristics of the contra-rotating axial flow pump–turbine in pump mode. Speed of the rear impeller was obtained for equal power operation of the two stages by adjusting the speed of rear

impeller. Thereafter, an analysis was conducted to determine the vorticity and blade load distribution of the rear impeller at different speeds. This research provides useful reference for the further study of the operation of the contra-rotating axial flow pump–turbine.

2. MATERIALS AND METHODS

2.1 Pump Geometry

In this paper, the design of the two-stage impellers is the same. Meanwhile, a two-way design, which no longer need to distinguish between flood and ebb modes in the later simulation process, is adopted for the impellers. The design parameters of the test pump are shown in

Table 1 Design parameters of the test pump

Design Parameters	Design value
Flow Q (m³/h)	160
Head H (m)	1.45
Rotating speed n (r/min)	1450
Blade numbers	3
Impeller hub diameter (mm)	48
Impeller shroud diameter (mm)	145

Blades are S-shaped airfoil and blade airfoil angles of the leading and trailing edges on the same contour planes are equal. Fig. 2 shows the blade airfoil angle on different contour planes β_1, β_2, β_3, β_4, and β_5, with values of 64.02º, 39.28º, 27.7º, 21.25º, and 17.11º, respectively.

The test pump is manufactured according to the proportion of design parameters to test and verify. The impeller mold is manufactured using 3D printing, as shown in Fig. 3. A protective ring was installed around the impeller to ensure the accuracy of the cast blade.
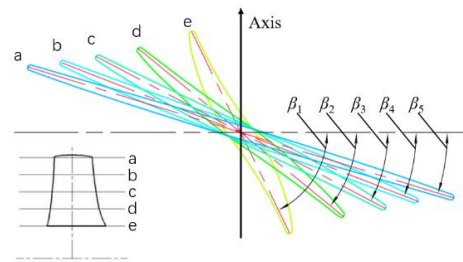

Fig. 2. Blade airfoil angles.

2.2 Experimental Methods

The experimental setup used in this research is a multi-functional testbed designed and built by the Fluid Mechanical Engineering Research Center of Jiangsu University and Jiangsu National Pump Co., LTD. Figure 4 shows the schematic of the experimental setup, including model pump, duffer tank, valves I and II (gate valve), and the related pipeline. In addition, relevant measuring instruments also include electromagnetic flowmeter and pressure sensor.

Fig. 3. Impeller mold.
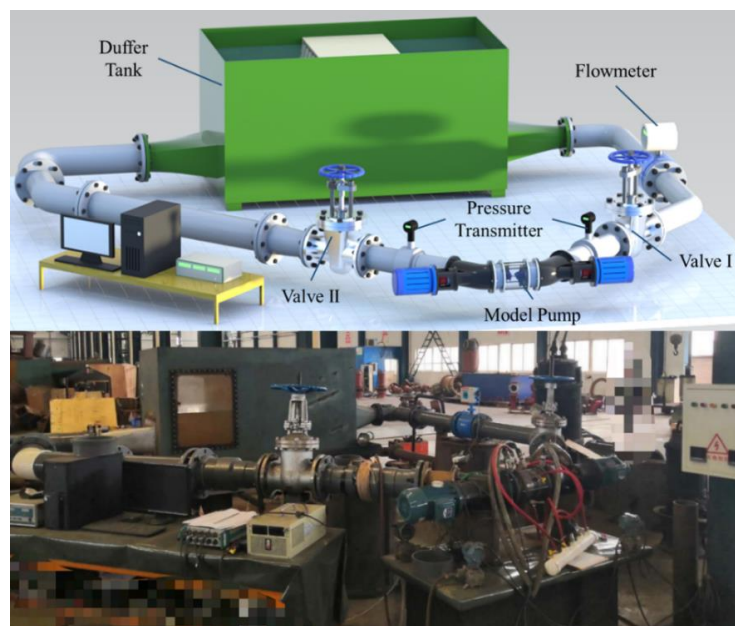
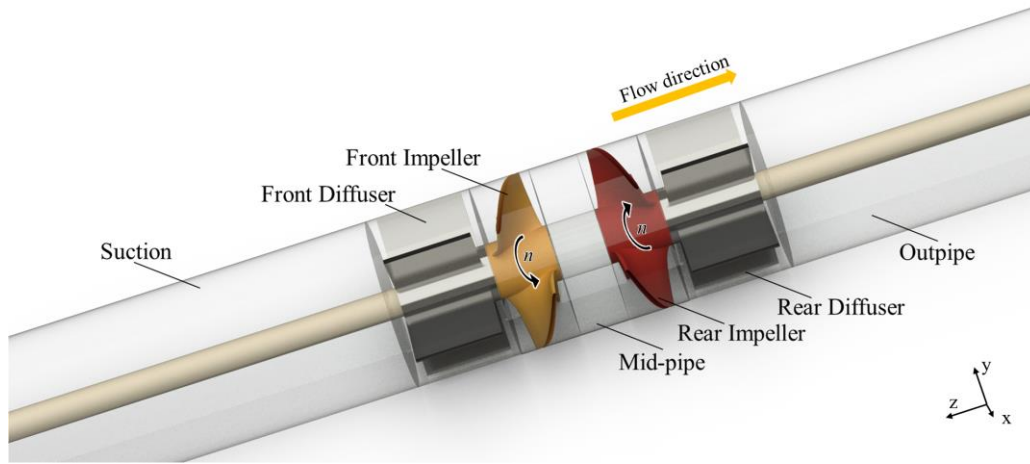**Fig. 4. Schematic of the experimental setup.**

Fig. 5. Domain of the hydraulic components.

Detailed parameters of each piece of equipment are as follows.

(1) WT3000-type pressure transmitter: −0.1 MPa to 0.5 MPa with a 0.2-level of accuracy.

(2) KEFC-type electromagnetic flowmeter: ±0.5% accuracy (flow rate ≥ 0.5 m/s).

(3) DT2243C-type photoelectric tachometer: 2.5 to 99,999 r/min range with a ±0.05% accuracy.

(4) BK8E-type three-phase multifunction energy meter: ±0.5% accuracy.

The total measurement error of the test system is as follows:

$$e = \sqrt[2]{0.5^2 + 0.2^2 + 0.05^2 + 0.5^2} = \pm 0.74\%$$

2.3 Numeral Methods

2.3.1 Hydraulic model components

Figure 5 shows the calculation model of the two-way contra-rotating axial flow pump. The computational domain includes the suction, front diffuser, front impeller, mid-pipe, rear impeller, rear diffuser, and outpipe. Note that the two-stage impellers have different rotational directions.

2.3.2 Meshing

ANSYS TurboGrid 2020 R2 is applied to mesh the impeller and the other component mesh is generated by the ANSYS ICEM. Tip clearance of the grid is set to 0.3 mm. Fig. 6 shows that grid independence analysis depends on the two-stage head in Q = 144 m³/h with a different number of grids. Head change is under 0.1% when the number of grids exceeds 5.2 million.

Figure 7 shows the mesh of the assembly and details of the impeller. A 10-layer grid (see Fig. 7 (c)) is used to divide the tip clearance region to obtain a better flow field. Figure 7 (e) shows the magnitude of y+ in the impeller wall. Flow in the mid-pipe, which is between the tow-stage impeller, is markedly complex, so the mesh in this region increases to a final count of 520,000.
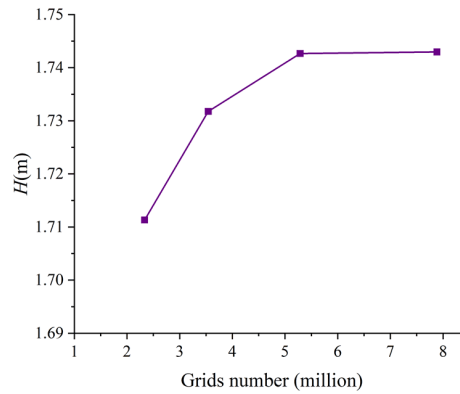

Fig. 6. Grid number of the test pump.

2.3.3 Calculation Method and Boundary Conditions

The RNG k-ε turbulence model is adopted for simulations. This model is one of the most widely used and validated turbulence models in industry. The RNG k-ε turbulence model can accurately predict the eddy under high strain-rate (Shao and Zhao 2019). The continuity and momentum equations are as follows (Zhang *et al.* 2020):

$$\frac{\partial u_i}{\partial x_i} = 0 \qquad (1)$$

$$\frac{\partial}{\partial t}\left(\rho \bar{u}_i\right) + \frac{\partial}{\partial x_j}\left(\rho \bar{u}_i \bar{u}_j\right)$$

$$= \frac{\partial}{\partial x_j}\left[\left(\mu + \mu_t\right)\frac{\partial \bar{u}_i}{\partial x_j}\right.$$

$$+ \mu_t\left(\frac{\partial \bar{u}_j}{\partial x_i} - \frac{2}{3}\delta_{ij}\frac{\partial \bar{u}_k}{\partial x_k}\right)\bigg] - \frac{\partial \bar{p}}{\partial x_i}$$

$$\qquad (2)$$

where p is the pressure, Pa; u_i is the velocity in the i direction, m/s; μ is the laminar dynamic viscosity, kg/(m·s); μ_T is the turbulent eddy dynamic viscosity, kg/(m·s); and ρ is 25 ℃ water density with a value of 997 kg/m³. The liquid phase is 25 ° C water and

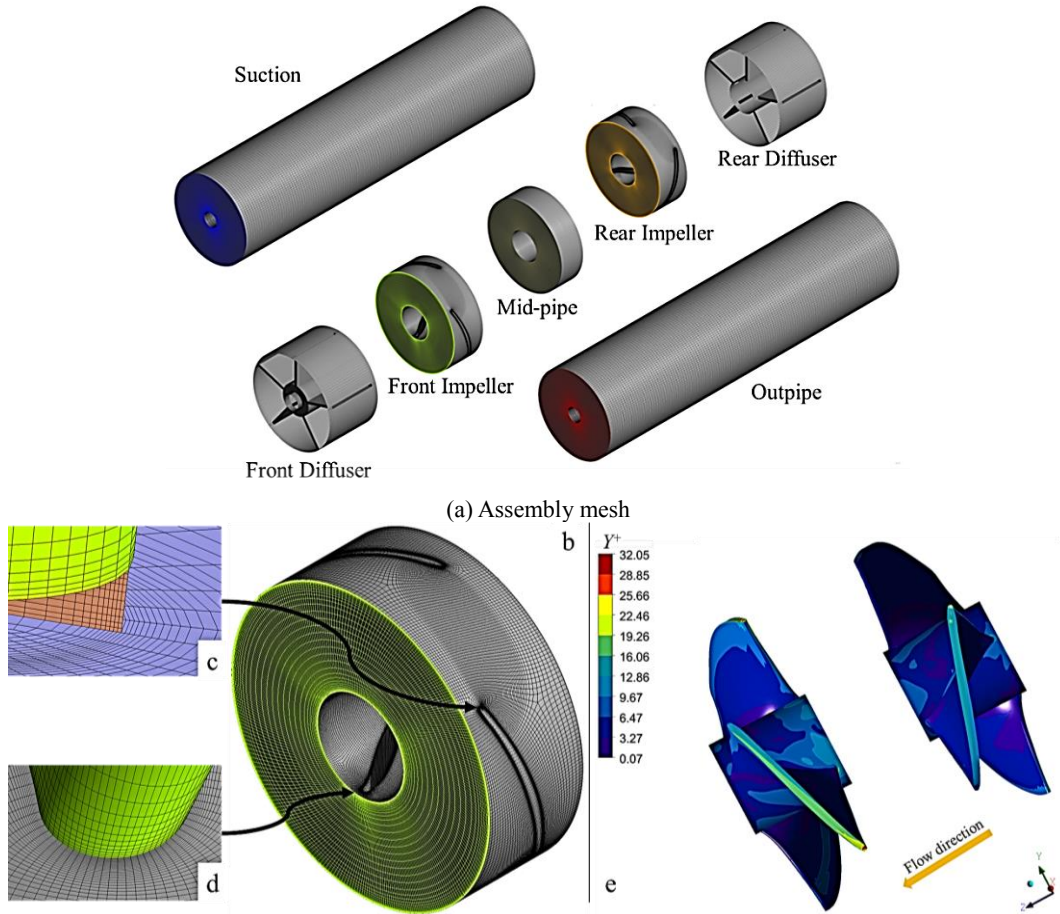(a) Assembly mesh

Fig. 7. Computational grids.

kinematic viscosity of 8.899×10^{-4} kgm^{-1}s^{-1}, and δ_{ij} is the Kronecker delta.

$$\delta_{ij} = \begin{cases} 1 & \text{for } i = j \\ 0 & \text{for } i \neq j \end{cases} \qquad (3)$$

The direction of rotation of the front and rear impellers is opposite. The calculation domain inlet is the normal speed inlet, and the outlet is set as average static pressure. No slip boundary conditions and smooth wall are used for the wall surfaces. Frozen rotor is used in interface set during the steady calculation. The residual target is set to 10^{-5}.

2.3.4 Vorticity equation

By considering the Navier–Stokes equation, the vorticity equation of the flow is as follows (Yu, 2016):

$$\frac{D\vec{\omega}}{Dt} = (\vec{\omega} \cdot \nabla)\vec{u} - \vec{\omega}(\nabla \cdot \vec{u})$$
$$+ \frac{\nabla\rho \times \nabla p}{\rho^2} + \nu\nabla^2\vec{\omega} \qquad (4)$$

where $\vec{\omega}$ is the vorticity, $\vec{u}$ is the velocity, ν is the kinematic viscosity, and ∇ is the Hamiltonian operator. On the right side of Eq. (3), each term represents vortex stretching, vortex dilatation, barotropic torque, and viscous diffusion. Given that the medium calculated in this paper is incompressible, the barotropic torque term equals 0. Reynolds number is large, its order of magnitude is about 10^6 near the blade tip, and the viscous diffusion term $\nu\nabla^2\vec{\omega}$ is relatively small to be typically disregarded. Thereafter, the Z-axis component of the vorticity equation is as follows:

$$\frac{D\vec{\omega}_Z}{Dt} = \left((\vec{\omega} \cdot \nabla)\vec{u}\right)_Z - \vec{\omega}_Z(\nabla \cdot \vec{u}) \qquad (5)$$

3. RESULTS AND DISCUSSIONS

3.1 Performance Test

Figure 8 shows the performance curve under pump mode obtained by experiment and numerical calculation. Note that the test results are slightly different from the results of the numerical calculation. The rotor–rotor interaction of the contra-rotating impellers is severe, and the internal flow is complex. Consequently, the instability of the pump flow field is increased, thereby leading to an increase in the prediction error of the steady-state numerical calculation of its head. However, numerical calculation results are consistent with the experimental results under full flow conditions. Therefore, the numerical results are comparatively reliable.
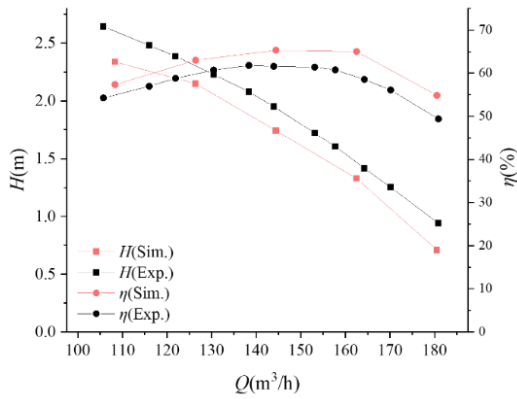
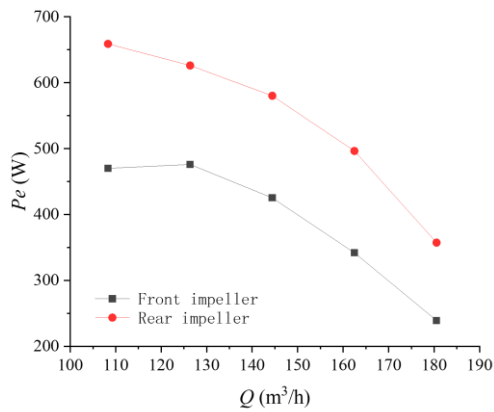**Fig. 8. Performance curve under pump mode.**

**Fig. 9. Performance curve of the equal-speed rotor.**

3.2 Research on the Rotational Speed under Pump Condition

The *Q-Pe* curve of the equal-speed rotor is shown in Fig. 9, where *Pe* is the shaft power of the impeller. The *Q-Pe* curves of the front and rear impellers are smoothly reduced. A large difference exists in shaft power between the two impellers at various flow conditions. Under varying flow rates, shaft power of the rear impeller is shown to be at least 31% higher compared with that of the front impeller.

As shown in Fig. 9, the two impellers maintain a regular variation in the entire flow condition range, but the rear impeller power is overpowered. Power mismatch of two-stage impellers is caused by the excessive difference between the blade inlet angle and inlet flow angle of the rear impeller. As pumps run in two-way, the same type of motor is used to drive impellers. Therefore, optimal power between the two impellers is equal. To reduce the power of the rear impeller, its speed is reduced to improve the inlet liquid flow angle.

To study the performance of the two-stage impeller separately, the head of each impeller should be analyzed in detail. Take the analysis of the front impeller as an example. Total pressure at the inlet and outlet interface of the front impeller is read separately, and total pressure difference is used to calculate the head of the front impeller. Given that flow at the interface is not markedly stable, even if the total pressure accessed is an average value,
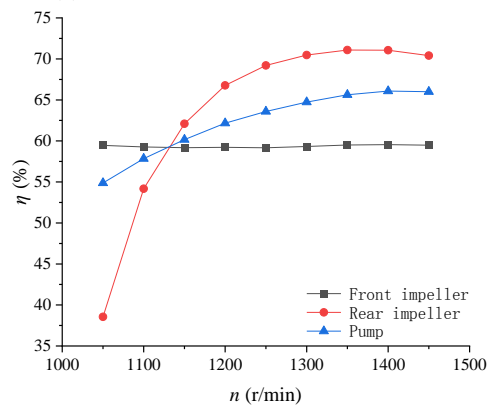
ensuring its accuracy remains difficult. Therefore, the head and efficiency of the single-stage impeller are used as reference parameters.
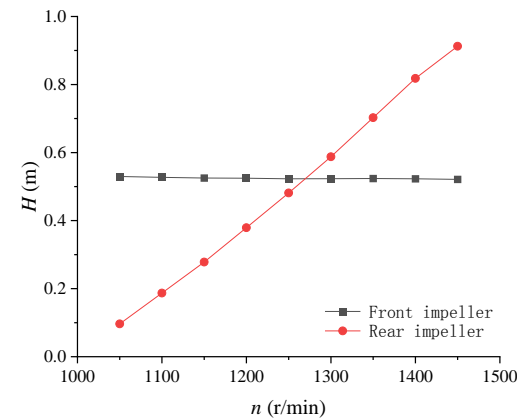
(a)
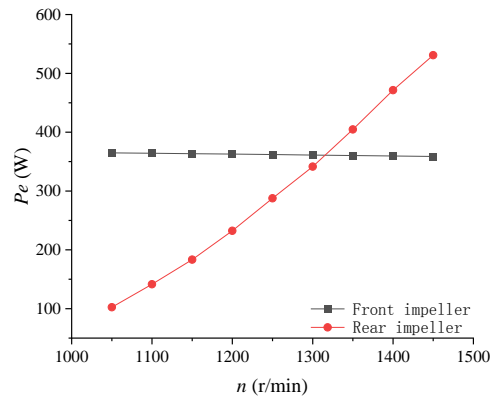
(b)

(c)

Fig. 10. Performance curve when *Q* = 160 m³/h.

Speed of the rear impeller is reduced by 50 r/min to research the pump performance when $Q = 160$ m³/h. Performance curve of the unit with the change of the rear impeller speed is shown in Fig. 10. The head, shaft power, and efficiency curve are shown in Fig. 10 (a)–(c), respectively. As the speed of the rear impeller decreases, the head and power of the rear impeller decrease in an approximately linear fashion. Moreover, the head and power of the front impeller remain nearly unchanged. The pattern of change of the efficiency curve differs from that of the other curves. Efficiency of the rear impeller first shows a

small increase followed by a rapid decrease. When the rear impeller speed decreased from 1450 r/min to 1300 r/min, efficiency will decrease by 1.34%. Furthermore, there will be a significant reduction in the head. Heads of the two impeller stages will be relatively similar when shaft powers are equal. Therefore, a single-stage impeller with half the total head is worth considering for the impeller design.

3.3 Streamline Analysis

Changes in flow pattern will have a significant impact on pump hydraulic performance and pump energy transfer characteristics (Li *et al.* 2020). In this case, flow pattern of the two impellers is studied, particularly in the area close to the leading edge (LE) of the rear impeller.

Span surface of the impeller is illustrated in Fig. 11, where Span 1 is span = 0.95 and Span 2 is span = 0.6. Therefore, the subsequent analysis revolves around equal speed and equal power. As shown in the curve in Fig. 10, powers of the two stages will be equal when the rear impeller reaches 1316 r/min. Therefore, simulation is performed again at a speed of 1316 r/min, which is referred to as the equal power condition.

Figure 12shows streamlines on the front and rear impellers Span 2 at varying rear impeller speeds. Figure 12(a) presents the streamline diagram of the front and rear impellers given equal speed, with no significant difference observed between equal speed and equal power. Figure 12(b) shows the streamline of the impeller given constant torque. Note that the red area indicates iso-surface with a flow velocity of 13 m/s.

By comparing Fig. 12 (a) and (b), note that the variation in flow velocity for the front and rear impellers under the context of equal power is similar
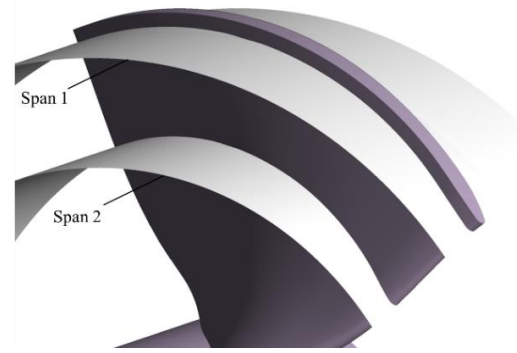

Fig. 11. Span surface.

to that under the contexts of constant torque and equal speed. The difference between the two lies in the inconsistent peak value of the high-speed area and inconsistent range of the high-speed area at the rear impeller LE. As shown in Fig. 12 (a), given equal speed, flow velocity of the front impeller is relatively high and concentrates at the trailing edge (TE) of the front impeller, thereby leading to a high-speed area. To further explore the flow characteristics of the rear impeller, velocity iso-surface of 13 m/s is extracted in this paper, as shown in Fig. 13. An area of higher speed accumulation is observed at the rear impeller LE, and the area in equal speed condition is found significantly larger than that in the equal power context. This situation is generally attributable to the work of the front impeller because the liquid flow angle near LE of the rear impeller will cease to be the same as that of the front impeller. When the rear impeller is reduced, the impact near LE is mitigated, as clearly evidenced by the reduction of the high-velocity area in this region. When the rear impeller's rotating speed is reduced,
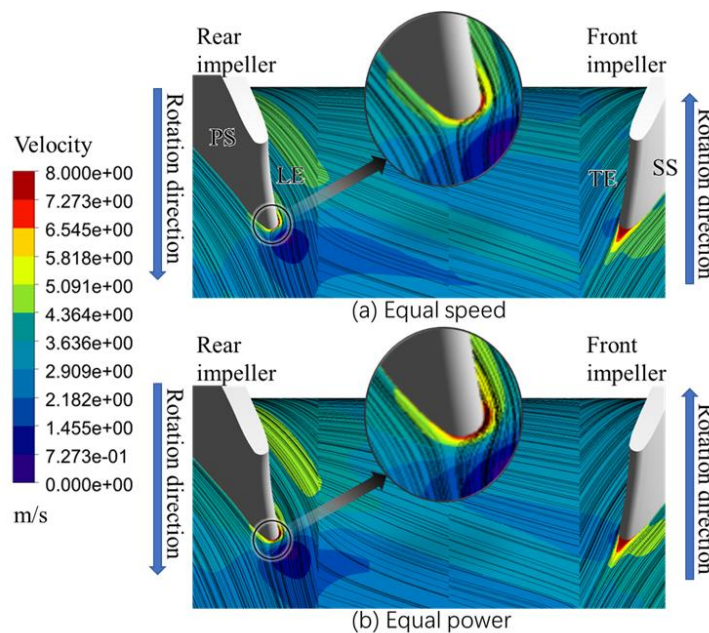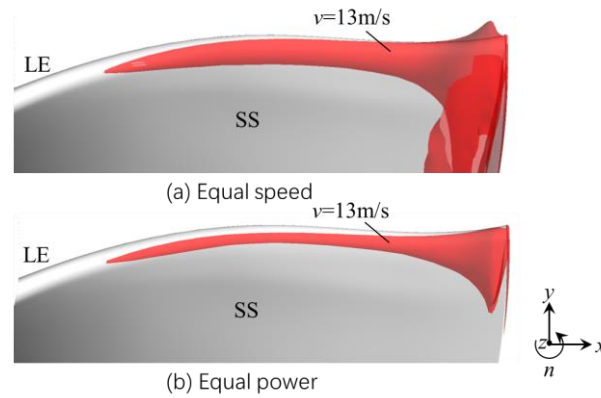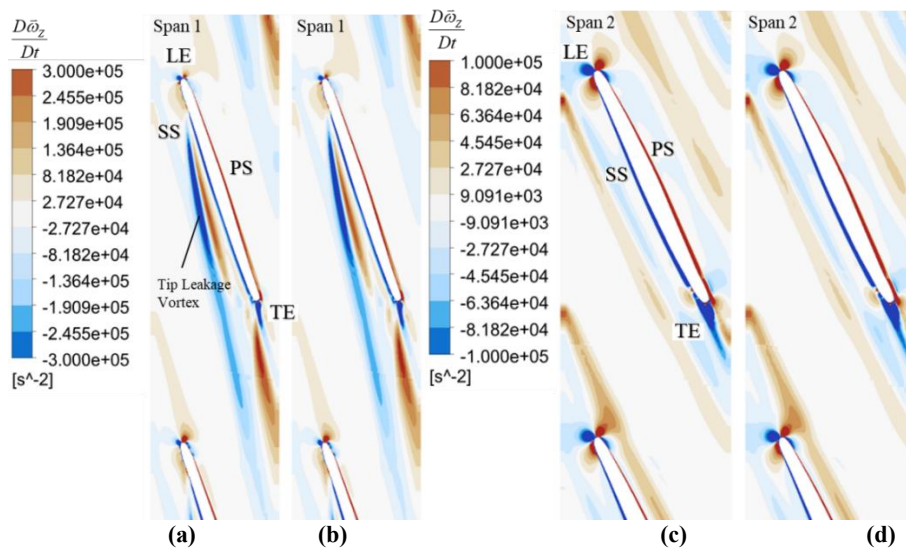

Fig. 12. Streamline on Span 2.

Fig. 13. Iso-surface set on the rear impeller blade.

Fig. 14 Contours of vorticity at the front impeller

the fluid impinging position on the rear impeller will change. In the basin near the suction surface (SS), flow rate decreases as the rear impeller rotating speed decreases.

3.4 Vorticity Analysis

Vortex characteristics can be used to further reveal the effects of changes in the rotational speed of the rear impeller on the vortex characteristics.

Figure 14 shows the vorticity distribution of the front impeller at different rear impeller speeds. In Fig. 14 (a) and (b), vorticity on Span 1 near the blade tip is shown. Note that the main vorticities are those caused by the LE impact, blade tip leakage, and wake near TE. Fig. 14 (c) and (d) show the vorticity of Span 2. In addition to the effects of the LE impact and impeller wake, wake of the front diffuser blade induces vorticities and will converge with those formed at the front impeller. As shown in Fig. 14, change in the rear impeller speed does not have a significant effect on vorticities inside the front impeller.

Figure 15(a) shows the distribution of vorticity on Span 1 of the rear impeller. SS of the blade is covered

with an area with a large absolute value of significant vorticity. The position close to SS is the gathering place of the positive value area, slightly further away from SS in the area caused by blade tip leakage. At the position where SS is close to TE, a longer wake begins to appear in the positive vorticity area attached to SS. A negative vorticity area also appears between the positive vorticity areas of the wake and tip leaking. Figure 15(b) shows contours of the vortex stretching term on Span 1, which is the same as that shown in Fig. 15 (a). In Fig. 15 (c), the vortex dilatation term is mainly found in the area of the tip leaking vortex. In addition, there are some in the vicinities of LE and TE of the blade and in the wake region. However, values of the vortex dilatation term in different regions are considerably small compared with the vortex stretching term.

Figure 16 shows contours of the vorticity and every term on Span 2 of the rear impeller under equal speed. In Fig. 16, vorticities on Span 2 are mainly flow separation caused by the LE impact water of the blades and vortices formed by the wake of the front impeller blades inducing the secondary blades on SS. Owing to the design of a large impeller inlet angle, vortices occur near the pressure surface (PS) on Span 2. Compared with Fig. 14 (c), this area of the rear impeller has a higher value than that of the front
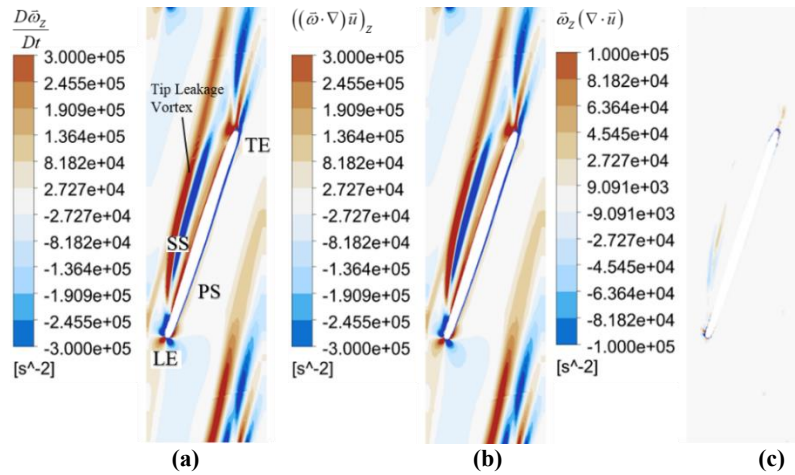
(a)   **(b)**   **(c)**

Fig. 15. Contours of vorticity and every term on Span 1 under equal speed.
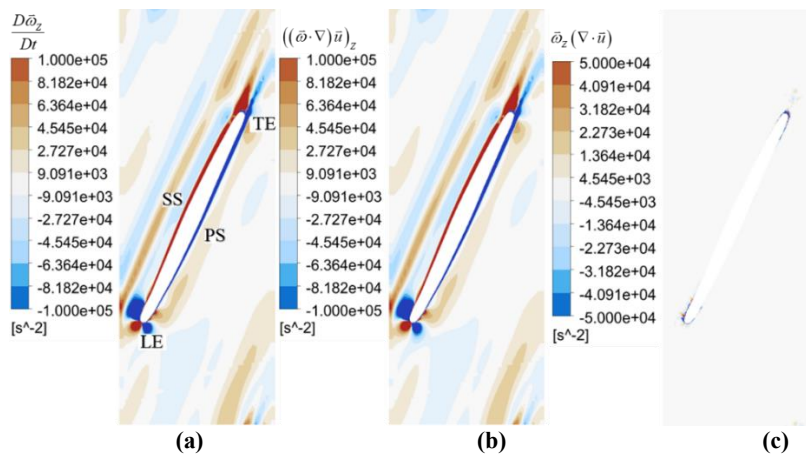

(a)   **(b)**   **(c)**

Fig. 16. Contours of vorticity and every term on Span 2 under equal speed.
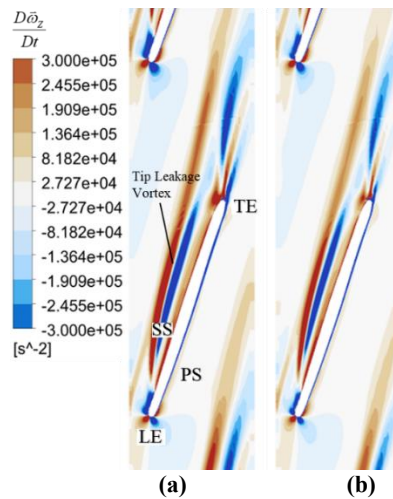

(a)   **(b)**

Fig. 17. Contours of vorticity on Span 1.

impeller. Identical to Fig. 15, contours of the vortex stretching term on Span 2 is the same as that shown in Fig. 16 (a). As shown in Fig. 16 (c), the vortex dilatation term distributes in the vicinities of LE and TE of the blade and in the wake region. Thereafter, analyzing the distribution of each term for the rear impeller at different speeds is no longer necessary.

Figures 17 (a) and (b) show the distributions of vorticity on Span 1 of the rear impeller under equal speed and equal power, respectively. Variations in the speed of the rear impeller can significantly affect the vortex structure. The positive value area caused by tip leakage decrease with the rear impeller speed decrease, and the phenomenon is more pronounced in the downstream region of TE. The wake region will also shrink as the rear impeller speed decreases.
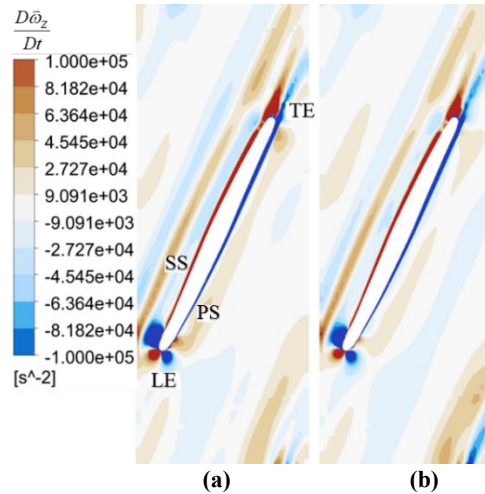
(a)   **(b)**
Fig. 18. Contours of vorticity on Span 2.

Figures 18(a) and (b) show the contours of vorticity on Span 2 of the rear impeller under equal speed and equal power, respectively. The positive value area near SS and PS decreases with a decrease in the rear impeller speed. The wake region will also shrink as the rear impeller speed decreases.

In summary, vorticity inside the front impeller does not change significantly as the speed of the rear impeller decreases. In this circumstance, however, there is a significant reduction in the vorticity within the rear impeller.

3.5 Blade Loading Analysis

Blade loading distributions of the span line of the rear impeller under different inlet pressures are shown in Fig. 19 (a)–(b). Span line is the intersection line between the span and blade surfaces.

As shown in Fig. 19, the value of Streamwise (S_{tr}) defines the location of the point corresponding to the pressure value, and its value is as follows:

$$S_{tr} = \frac{R - R_1}{R_2 - R_1} \qquad (6)$$

Figure 19(a) shows the blade loading distributions of the Span 1 line. LE impact leads a large pressure fluctuation on the surface near LE. In SS near LE, a low-pressure area occurs, and pressures reach −159.0 kPa and −151.7 kPa. In PS near LE, a high-pressure area occurs. In PS of $0.304 < S_{tr} < 0.843$ and SS of $0.126 < S_{tr} < 0.765$, the pressure curve is almost maintained at a fixed value. As the wake appears first in the area of SS near TE, there is a slight decline in pressure. At PS, pressure variation at different speeds is not significant. In SS, pressure variation caused by the different rotational speeds is extremely pronounced.

Figure 19(b) shows the blade loading distributions of the Span 2 line. A contour of pressure distribution in the area near the blade was also added to Fig. 19 (b). In SS near LE, a low-pressure area occurs, and pressures reach −117.6 kPa and −87.8 kPa. In PS near LE, a high-pressure area occurs. In PS of $0.183 < S_{tr} < 0.891$, pressure varies within a small range. In
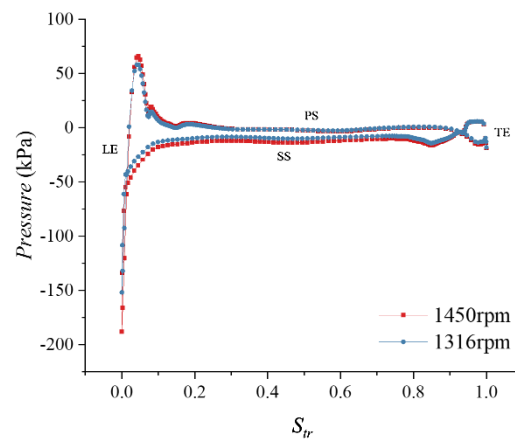
(a) Span 1 line
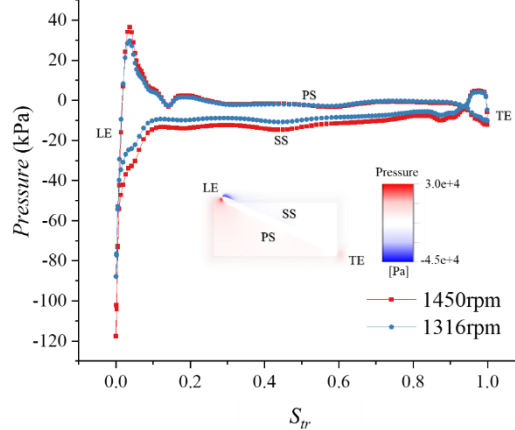
(b) Span 2 line
Fig. 19. Blade loading distributions.

SS of $0.12 < S_{tr} < 0.838$, the pressure curve gradually increases from LE to TE. Some small fluctuations in pressure are observed in the middle of SS, which is caused by a large twist S-sharp in the Span 2 line. Similar to the Span 1 line, pressure variation caused by the different rotational speeds is extremely pronounced in SS.

As shown in Fig. 19, pressures in the central part of PS nearly coincide, which is due to the fact that the outlet is set as average static pressure within the

calculation. As the rear impeller speed decreases, low pressures increase considerably at SS near LE. In addition, pressure difference between PS and SS decreases at different span lines. This condition is reflected in the external characteristics of the pump, which is the reduction in the head and shaft powers.

4. CONCLUSIONS

The performance of two-stage impellers under pump mode is analyzed to reveal a significant power difference between the two-stage impellers, with the rear impeller found susceptible to motor overload. By reducing the speed of the rear impeller, the matching speed of the two-stage impellers with equal-power operation is determined, and the internal flow phenomenon of the rear impeller is investigated. On this basis, the following conclusions are drawn.

(1) Under the context of equal-speed operation, the power of rear impeller under the pump mode reaches an exceptionally high level, which is inconsistent with the power of the front impeller. As speed of the rear impeller decreases, the head and power of the rear impeller show a decreasing trend almost linearly. As the speed of the rear impeller declines, the head and power of the rear impeller diminish almost linearly. Efficiency of the rear impeller first shows a slight increase before a rapid decrease. When the rear impeller speed is reduced from 1450 r/min to 1300 r/min, efficiency decreases by 1.34%.

(2) Vorticity within the front impeller shows no significant change as the speed of the rear impeller decreases. However, there is a sharp decline in vorticity within the rear impeller. Judging from the vortex structure on the span = 0.95, tip leakage vortex inevitably occurs. As rotation speed of the rear impeller decreases, vortex structure remains unchanged despite a reduction in the vorticity value.

(3) As the speed of rear impeller decreases, variation in pressure between PS and SS is reduced in different span lines. Owing to the leading edge impact, there is a significant fluctuation of pressure on the surface near LE. In SS near LE, a low-pressure area develops. The value of this area also increases considerably when the rear impeller speed decreases.

In this paper, the rotor–rotor interaction of the contra-rotating impellers reaches a significant extent and the internal flow shows complexity, which makes the prediction error of the steady-state numerical calculation markedly significant. In future studies, the characteristics of performance produced under unsteady conditions at different rear impeller speeds should be explored. By analyzing the blade load distribution of the rear impeller span line under different inlet pressures at different span positions, pressure changes caused by different rotational speeds are evident in SS of the rear impeller.

As the speed of the rear impeller declines, low rear pressures increase sharply at SS near LE. In addition, pressure difference between PS and SS is reduced at different span lines, as reflected in the external characteristics of the pump, thereby resulting in the reduction of head and the shaft power. Therefore, this research provides a practical reference for the further study of the operation of the contra-rotating axial flow pump-turbine.

DECLARATION OF CONFLICTING INTERESTS

The author(s) declared no potential conflicts of interest with respect to the research, authorship, and/or publication of this article.

REFERENCE

Ai, Z., G. Qin, W. He and X. Chen (2016). Speed matching of two-stage impeller with counter-rotating fan under variable operating conditions. *Journal of Harbin Engineering University* 37(4) 592-597.

Ai, Z., G. Qin, J. Lin, X. Chen and W. He. (2017). Speed Matching for Second Impeller with Equal Power of Two-Stage Impellers of Counter-Rotating Fan. *Journal of Xi'an Jiaotong University* 51(3), 1-6.

Angeloudis, A. and R. A. Falconer (2017). Sensitivity of tidal lagoon and barrage hydrodynamic impacts and energy outputs to operational characteristics. *Renewable Energy* 114, 337-351.

Burrows, R., I. Walkington, N. C. Yates, T. S. Hedges, J. Wolf and J. T. Holt (2009). The tidal range energy potential of the West Coast of the United Kingdom. *Applied Ocean Research* 31(4), 229-238.

Cao, L., S. Watanabe, T. Imanishi, H. Yoshimura and A. Furukawa (2013). Experimental analysis of flow structure in contra-rotating axial flow pump designed with different rotational speed concept. *Journal of Thermal Science* 22(4), 345-351.

Charlier, R. H. (2003). A "sleeper" awakes: tidal current power. *Renewable and Sustainable Energy Reviews* 7(6), 515-529.

Clarke, J. A., G. Connor, A. Grant and C. Johnstone

(2007). Design and testing of a contra-rotating tidal current turbine. *Proceedings of the Institution of Mechanical Engineers, Part A: Journal of Power Energy* 221(2), 171-179.

Clarke, J. A., G. Connor, A. Grant, C. Johnstone and S. Ordonez Sanchez (2009). Contra-rotating marine current turbines: single point tethered floating system-stabilty and performance. *8th European Wave and Tidal Energy Conference*, EWTEC 2009,

Denantes, F. and E. Bilgen (2006). Counter-rotating turbines for solar chimney power plants. *Renewable Energy* 31(12), 1873-1891.

Furukawa, A., T. Shigemitsu and S. Watanabe (2007). Performance test and flow measurement of contra-rotating axial flow pump. *Journal of Thermal Science* 16(1), 7-13.

Furukawa, A., S. Usami, Y. Tsunenari, S. Watanabe and K. Okuma (2009). Limiting Streamlines Measurement in Contra-Rotating Axial Flow Pump. In *Proceedings of the 4th International Symposium on Fluid Machinery and Fluid Mechanics,* Berlin, Germany, 161-166, Springer.

Harcourt, F., A. Angeloudis and M. D. Piggott (2019). Utilising the flexible generation potential of tidal range power plants to optimise economic value. *Applied Energy* 237, 873-884.

Kim, K., M. R. Ahmed and Y. Lee (2012). Efficiency improvement of a tidal current turbine utilizing a larger area of channel. *Renewable Energy* 48, 557-564.

Kim, S.-J., H.-M. Yang, J. Park and J.-H. Kim (2022). Investigation of internal flow characteristics by a Thoma number in the turbine mode of a Pump–Turbine model under high flow rate. *Renewable Energy* 199, 445-461.

Li, C. (2016). *The Study of internal flow field and impeller static characteristic under Variable Speed on Contra-Rotating Fan* Harbin University of Science and Technology].

Li, X., B. Chen, X. Luo and Z. J. R. E. Zhu (2020). Effects of flow pattern on hydraulic performance and energy conversion characterisation in a centrifugal pump. *Renewable Energy* 151, 475-487.

Li, Y., B. J. Lence and S. M. Calisal (2011). An integrated model for estimating energy cost of a tidal current turbine farm. *Energy Conversion Management* 52(3), 1677-1687.

Liu, H. R., S. J. Geng, H. A. Fang and C. Q. Nie (2012). Numerical study on matching performance of contra-rotating axial flow fan under variable speed. Machinery Design & Manufacture *3, 116-118.*

Mackay, D. J. C. and D. Hafemeister (2010). Sustainable Energy-Without the Hot Air. *American Journal of Physics* 78(2), 222-223.

Mao, X., X. Chen, J. Lu, P. Liu and Z. Zhang (2022).

Improving internal fluid stability of pump turbine in load rejection process by co-adjusting inlet valve and guide vane. *Journal of Energy Storage* 50, 104623.

Mistry, C. and A. Pradeep (2013). Effect of variation in axial spacing and rotor speed combinations on the performance of a high aspect ratio contra-rotating axial fan stage. *Proceedings of the Institution of Mechanical Engineers, Part A: Journal of Power Energy* 227(2), 138-146.

Mistry, C. and A. Pradeep (2014). Influence of circumferential inflow distortion on the performance of a low speed, high aspect ratio contra rotating axial fan. *Journal of Turbomachinery* 136(7), 071009.

Neill, S. P., A. Angeloudis, P. E. Robins, I. Walkington, S. L. Ward, I. Masters, M. J. Lewis, M. Piano, A. Avdis and M. D. Piggott (2018). Tidal range energy resource and optimization – Past perspectives and future challenges. *Renewable Energy* 127, 763-778.

Prandle, D. (1984). Simple theory for designing tidal power schemes. *Advances in Water Resources* 7(1), 21-27.

Qian, P., B. Feng, H. Liu, X. Tian, Y. Si and D. Zhang (2019). Review on configuration and control methods of tidal current turbines. *Renewable and Sustainable Energy Reviews* 108, 125-139.

Ravelet, F., F. Bakir, C. Sarraf and J. Wang (2018). Experimental investigation on the effect of load distribution on the performances of a counter-rotating axial-flow fan. *Experimental Thermal and Fluid Science* 96, 101-110.

Sangiuliano, S. J. (2017). Community energy and emissions planning for tidal current turbines: A case study of the municipalities of the Southern Gulf Islands Region, British Columbia. *Renewable Sustainable Energy Reviews* 76, 1-8.

Shao, X. and W. Zhao (2019). Performance study on a partial emission cryogenic circulation pump with high head and small flow in various conditions. *International Journal of Hydrogen Energy* 44(49), 27141-27150.

Shigemitsu, T., T. Takano, A. Furukawa, K. Okuma and S. Watanabe (2005). Pressure measurement on casing wall and blade rows interaction of contra-rotating axial flow pump. *Journal of Thermal Science* 14(2), 142-149.

Stuermer, A. W. and R. A. Akkermans (2014). Validation of aerodynamic and aeroacoustic simulations of contra-rotating open rotors at low-speed flight conditions. *In 32nd AIAA applied aerodynamics conference, Atlanta, USA, 16-20, the American Institute of Aeronautics and Astronautics.*

Sun, X. (2018). *Study on the Electromechanical Performance Matching and Pole-Changing Control for Two Drive Motors of the Contra-Rotating Fan* Ph. D. thesis, Harbin University

of Science and Technology, Harbin, China.

Tiwari, G., J. Kumar, V. Prasad and V. Patel (2022). CFD Investigation for Surface Roughness Effects on the Hydrodynamics of Cavitating Turbulent Flow through a Low Head Prototype Francis Turbine. *Journal of Applied Fluid Mechanics* 15(5), 1593-1607.

Xia, J., R. A. Falconer and B. Lin (2010). Impact of different tidal renewable energy projects on the hydrodynamic processes in the Severn Estuary, UK. *Ocean Modelling* 32(1), 86-104.

Yates, N., I. Walkington, R. Burrows and J. Wolf (2013). The energy gains realisable through pumping for tidal range energy schemes. *Renewable Energy* 58(10), 79-84.

Yu, A., L. Li, J. Ji and Q. Tang (2022). Numerical study on the energy evaluation characteristics in a pump turbine based on the thermodynamic entropy theory. *Renewable Energy* 195, 766-779.

Yu, A., D. Zhou and Y. Wang (2021). Vortex Evolution and Energy Production in the Blade Channel of a Francis Turbine Operating at Deep Part Load Conditions. *Journal of Applied Fluid Mechanics* 14(6), 1669-1678.

Yu, Z. (2016). *Numerical and Physical investigation of Tip Leakage Vortex Cavitating Flows* Ph. D. thesis, Beijing Institute of Technology, Beijing, China.

Zhang, F., D. Appiah, F. Hong, J. Zhang, S. Yuan, K. A. Adu-Poku and X. Wei (2020). Energy loss evaluation in a side channel pump under different wrapping angles using entropy production method. *International Communications in Heat and Mass Transfer* 113, 104526.

Zhang, Z. (2015). *The Study of Blade Aerodynamics Characteristics under Variable Speed on Contra-Rotating Fan.* Master's thesis, Harbin University of Science and Technology, Harbin, China.